ELSEVIER

Contents lists available at ScienceDirect

Water Research

journal homepage: www.elsevier.com/locate/watres



Equivalent film-electrode model for flow-electrode capacitive deionization: Experimental validation and performance analysis



Li Wang ^a, Changyong Zhang ^b, Calvin He ^b, T. David Waite ^b, Shihong Lin ^{a, c, *}

- ^a Department of Civil and Environmental Engineering, Vanderbilt University, Nashville, TN, 37235-1831, USA
- b UNSW Water Research Centre, School of Civil and Environmental Engineering, The University of New South Wales, Sydney, New South Wales, 2052, Australia
- ^c Department of Chemical and Biomolecular Engineering, Vanderbilt University, Nashville, TN, 37235-1604, USA

ARTICLE INFO

Article history: Received 23 December 2019 Received in revised form 26 April 2020 Accepted 3 May 2020 Available online 15 May 2020

ABSTRACT

Flow electrode capacitive deionization (FCDI) is a promising configuration for capacitive deionization due to its capability of continuous operation and achieving a relatively large salinity reduction. Due to the complexity of the multi-phase flow involved in FCDI, modeling FCDI system performance has been a challenge with no predictive FCDI model thus far developed. In this study, we developed an equivalent film-electrode (EFE) model for FCDI in which the flow electrodes are approximated as moving film electrodes that behave in a manner similar to conveyor belts. The EFE-FCDI model is validated using results from a series of FCDI experiments and then applied to elucidate the spatial variations of the key properties of the FCDI system and to resolve the contributions of different aspects of the system to energy consumption. The impact of activated carbon loading in the flow electrode and the feed and effluent target concentrations on the overall FCDI performance are also discussed based on model simulation. In summary, the EFE-FCDI model enhances our understanding of the system-level behavior of FCDI systems and can be employed for optimizing FCDI design and operation.

© 2020 Elsevier Ltd. All rights reserved.

1. Introduction

Capacitive deionization (CDI), also referred to as electrosorption, is an emerging electrochemical desalination technology of particular current interest in view of its potential to become a competitive technology in certain desalination applications (Porada et al., 2013a; Suss et al., 2015). With carbonaceous electrodes, CDI involves the removal of ions from the feed stream and storage of these ions in the electrode micropores when a voltage is applied, with subsequent release of the stored ions into the brine stream when the electrodes are short-circuited or a reverse voltage is applied(Farmer et al., 1996; Porada et al., 2013b; Ji et al., 2019; Tang et al., 2019a). There are a variety of CDI cell configurations and operational modes(Porada et al., 2014; Zhao et al., 2012; Suss et al., 2012; Wang and Lin, 2018a; Tang et al., 2019b), among which flow electrode CDI (FCDI) has received extensive and growing interest(Zhang et al. 2018, 2019, 2020; Jeon et al., 2013; He et al., 2018a;

E-mail address: shihong.lin@vanderbilt.edu (S. Lin).

Cho et al., 2019; Luo et al., 2020). Three major advantages of FCDI over other CDI configurations include (i) the ability of continuous operation(Jeon et al., 2014; Gendel et al., 2014; Rommerskirchen et al., 2018a) compared to cyclic operation in conventional CDI that is more difficult to control and optimize; (ii) the possibility of achieving a high degree of salinity reduction(Jeon et al., 2014; Yang et al., 2016; Moreno and Hatzell, 2018); and (iii) extremely high flow efficiency (~100%) as it avoids the switch between the desalinated and brine streams in the flow channel (Rommerskirchen et al. 2015, 2018a; Hawks et al., 2018a).

In FCDI, flow electrodes comprising a slurry mixture of activated materials (i.e., activated carbon, AC), conductive additives (e.g., carbon black particles, carbon nanotubes and redox couples) and aqueous electrolyte are pumped through two electrode channels while the salty feed water flows through the spacer channel(Liang et al., 2017; Hatzell et al., 2015; Ma et al., 2019). Typically, ion exchange membranes are employed to separate the electrode channels from the spacer channel. There are two general modes in which FCDI may be operated, namely, the short-circuited closed-cycle (SCC) operation and the isolated closed-cycle (ICC) operation (Jeon et al., 2014; Yang et al., 2017). In ICC mode, the positively and negatively charged flow electrodes are isolated and recirculated

^{*} Corresponding author. Department of Civil and Environmental Engineering, Vanderbilt University, Nashville, TN, 37235-1831, USA.

between their respective electrode channels and electrode reservoirs. Similar to conventional CDI, ICC-FCDI is an intermittent process as it requires that the flow electrodes be regenerated by applying a reverse voltage. In contrast, a continuous, steady-state FCDI operation can be achieved using SCC operation. In SCC operation, the flow electrodes are regenerated when the positively and negatively charged AC slurries exiting the FCDI cell are mixed together in a single reservoir (Fig. 1A). The contact between these oppositely charged AC particles results in neutralization of the AC and release of the adsorbed ions to the electrolyte solution that becomes the brine.

Recent advances in film-electrode based CDI, i.e. CDI systems using solid phase thin-film electrodes, can be attributed, in part, to the enhanced fundamental understanding that has accrued from the development of dynamic CDI models. The ability to model the behavior of CDI systems is critical to understanding the impacts of system parameters and operating conditions on CDI performance and for optimizing CDI system design and operation(Wang and Lin, 2018a, 2019, 2018b; Wang et al., 2017; Wang et al., 2020). Models with different levels of fidelity have been developed for filmelectrode CDI(Hemmatifar et al., 2015; Biesheuvel et al., 2011; He et al., 2018b; Suss et al., 2014; Qin et al., 2019), however, very limited effort has been devoted to the modeling of FCDI. The major challenge in modeling FCDI is the treatment of the dynamic percolation between AC particles in the complex multi-phase flow electrode(Karzar-Jeddi et al., 2019), which is dependent on AC loading and flow characteristics(Dennison et al., 2014).

The only FCDI model that has been reported is that by Rommerskirchen et al. where they discretized the FCDI cell in the flow direction and coupled ion transport with the modified Donnan (mD) model for description of the electrical double layer (EDL) (Rommerskirchen et al., 2018b). However, the use of the Stern layer capacitance as a fitting parameter that varies in different operations is not only physically ungrounded but also undermines the predictive power of the model (i.e., while this model can be used for fitting experimental data, it cannot be used for predicting performance). For example, increasing AC loading in the flow electrode promotes more frequent collision of AC particles and thus enhances the conductivity of the flow electrode. However, this effect of increasing AC loading is incorrectly accounted for by changing the Stern layer capacitance. In contrast, previous studies on fixed electrode CDI with AC film electrodes have revealed that the Stern layer capacitance is dependent on the micropore charge density via the mechanism of electrostatic compression (Bazant et al., 2005; Grahame, 1947), but not directly dependent on any other operating condition.

We demonstrate in this study that the system-level behavior of FCDI can be approximately modelled by an equivalent CDI model of moving film electrodes without the need for considering the mechanistic details of inter-particulate mass and charge transfer (Fig. 1B). Specifically, a flow electrode stream can be approximated as a film electrode with much larger macro-pore volume and significantly reduced electrical conductivity. Such an equivalent film electrode (EFE) moves in the direction of the flow in a manner similar to a "conveyer belt". Following this approximation, we develop a pseudo-1D model that describes the ion transport and the EDL formation in the FCDI with appropriate treatment of the Stern layer capacitance and the effect of AC loading. This pseudo-1D equivalent film electrode (EFE) model is validated using FCDI experiments in SCC mode and is then employed to evaluate the FCDI performance over a wide range of operating conditions. In addition, the EFE-FCDI model developed here is used to describe the spatial distribution of the important properties in the FCDI cell and the breakdown of the energy losses in the system. Finally, we employ the developed EFE-FCDI model to conduct an analysis of the performance tradeoff in FCDI.

2. Model development

2.1. System description

In this section, we present the governing equations of a pseudo-1D EFE model that describes ion transport in the spacer channel and ion retention in the electrode channel. Both the spacer and the electrode channels are divided into *N* subcells connected in series, each of which is assumed to be a continuously stirred-tank reactor (CSTR). The electrode channel consists of AC particles with intraparticulate macropores and micropores. The volume occupied by the electrolyte solution outside the AC particles is considered as a large "extra-particulate macropore". In the EFE-FCDI model, intraparticulate and extra-particulate macropores are not distinguished and have the same ion concentration. Based on existing film-electrode CDI models, micropores contribute to the majority of ion storage capacity while macropores serve as pathways for rapid ion transport.

2.2. Ion transport in a unit cell

As the spacer channel is discretized into *N* sub-cells in series, the mass balance of salt in each CSTR-like subcell can be expressed as:

$$p_{sp}V\frac{\partial c_{sp,k}}{\partial t} = -J_{salt,k}A + Q_{sp}\left(c_{sp,k-1} - c_{sp,k}\right)$$
(1)

where p_{sp} is the spacer porosity, V is the volume (mL) of the subcell, $c_{sp,k}$ is the spacer channel concentration (mol mL⁻¹) in subcell k, $J_{salt,k}$ is the salt flux (mol cm⁻² s⁻¹) from the spacer channel toward the electrode channel in sub-cell k (same as the ion fluxes $J_{ions,k}$), A is the effective contact area (cm²) between the spacer and the

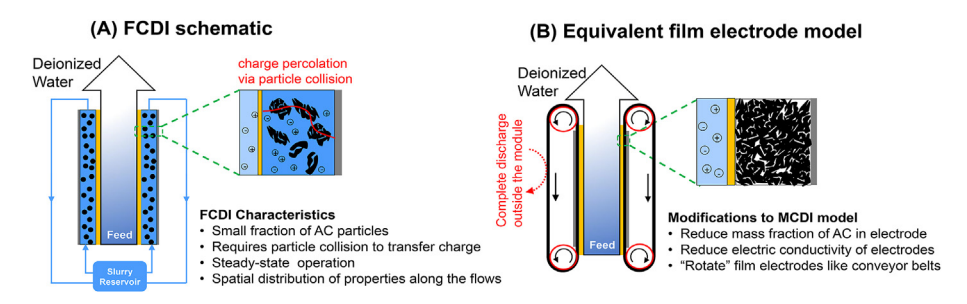


Fig. 1. (A) Schematic of the FCDI system operating in short-circuited closed-cycle (SSC) mode. (B) the equivalent film-electrode model in which the film electrodes behave as conveyor belts that rotate through the FCDI module. The major characteristics of the FCDI system are listed in (A) and the corresponding measures for modifying the MCDI model to account for such characteristics are lised in (B).

electrode channels, and Q_{sp} is the stream flowrate (mL s⁻¹) in the spacer channel. The transport of ions across the respective IEM is driven by the gradients of both electrical potential and concentration. The flux (mol cm⁻² s⁻¹) of ion species i, $J^i_{ions,k}$, in sub-cell k can be described by the Nernst-Planck equation:

$$J_{ions,k}^{i} = -D_{m} \left(\frac{\partial c_{m,k}^{i}}{\partial x} + z^{i} c_{m,k}^{i} \cdot \frac{\partial \varphi_{m,k}}{\partial x} \right)$$
 (2)

where D_m is the diffusion coefficient (cm 2 s $^{-1}$) in the IEM (D_m is ion-specific in principle but, in this model, we use the mean diffusion coefficient of the salt), $c_{m,k}^i$ is the concentration (mol mL $^{-1}$) of i in the IEM of subcell k, and $\varphi_{m,k}$ is the dimensionless electrical potential in the IEM of subcell k. Due to the requirement for local electro-neutrality in the membrane, the following equation applies:

$$c_{m\,k}^{+} - c_{m,k}^{-} + \omega X = 0 \tag{3}$$

where $c_{m,k}^+$ and $c_{m,k}^-$ are concentrations (mol mL⁻¹) of cation and anion in the IEM of subcell k, respectively, X is the intrinsic charge density (mol mL⁻¹) of IEM and ω is the sign of the charge (i.e., -1 for cation exchange membrane, CEM, and +1 for anion exchange membrane, AEM).

Considering both cation and anion fluxes by adding equations (2) and (3) with the simplifying assumption of linear gradients for concentration and electrical potential across the IEM, we arrive at the following equation:

$$J_{ions,k} = -\frac{D_m}{L_m} \left(\Delta c_{m,k} - \omega X \Delta \varphi_{m,k} \right) \tag{4}$$

where L_m is the thickness of the membrane (cm) and $\Delta c_{m,k}$ is the difference in total ion concentrations (i.e., $c_{m,k} = c_{m,k}^+ + c_{m,k}^-$, unit:mol mL⁻¹) between the two edges of the IEM. Here, the edge refers to the IEM phase that is next to the interface. In other words, $\Delta c_{m,k} = c_{m/elec,k} - c_{m/sp,k}$ with $c_{m/elec,k}$ being the IEM-phase total ion concentration (mol mL⁻¹) next to the interfaces between the IEM and the electrode channel of subcell k, and $c_{m/sp,k}$ being the IEM-phase total ion'concentration (mol mL⁻¹) at the interfaces between the IEM and the spacer channel of subcell k. The IEM-phase concentrations near the interface are related to the solution concentrations near the interface in a manner reasonably described by the following expressions:

$$c_{m/elec,k} = 2c_{mA,j}\cosh\left(\Delta\varphi_{m/e,k}\right) \tag{5}$$

$$c_{m/sp,k} = 2c_{sp,j}\cosh\left(\Delta\varphi_{m/sp,k}\right) \tag{6}$$

where $c_{mA,k}$ and $c_{sp,k}$ are macropore and spacer concentrations (mol mL⁻¹) in subcell k and $\Delta \varphi_{m/e,k}$ and $\Delta \varphi_{m/sp,k}$ are the Donnan potentials across the electrode/IEM and spacer/IEM interfaces in subcell k, respectively.

The current density (A cm⁻²) of subcell k, I_k , depends on the electrical potential difference across the spacer channel and the spacer salt concentration:

$$I_{k} = -2Dc_{sp,k} \frac{\Delta \varphi_{hf-sp,k}}{L_{sp}/2} F \tag{7}$$

where *D* is the bulk diffusion coefficient (cm² s⁻¹) of the charged ions (we use the mean diffusion coefficient of the salt here), $\Delta \varphi_{hf-sp,k}$ is the dimensionless potential drop of half of the spacer

channel of subcell k, $L_{sp}/2$ is half of the spacer thickness (cm) and F is the Faraday constant (96,485 C mol⁻¹). Eq (7) assumes that the suspension in the spacer volume in subcell k is completely mixed and thus has no concentration gradient. Because the current density in the spacer equals that in the IEM, it can be quantified as shown in Eq. (8):

$$I_{k} = -D_{m}\overline{c}_{m,k}\frac{\Delta\varphi_{m,k}}{L_{m}}F\tag{8}$$

where $\bar{c}_{m,k}$ is the average ion concentration (mol mL⁻¹) in the IEM in subcell k.

2.3. Ion partitioning between micropores and macropores

Upon charging, electrical double layers (EDLs) overlap substantially inside the micropores of the AC, which renders the modified Donnan (mD) approximation applicable for describing the ion distribution between micropores and macropores in each subcell(Biesheuvel et al., 2011). The mD model assumes a constant potential inside the micropore and thus a single potential difference between the micro- and macro-pores (i.e., the dimensionless Donnan potential in subcell k, $\Delta \varphi_{D,k}$). The ratio of the concentration (mol mL⁻¹) of a specific ion i in the micropore, $c_{mi,k}^i$, and the concentration (mol mL⁻¹) of the same ion in the macropore, $c_{mA,k}^i$, is governed by $\Delta \varphi_{D,k}$ via the Boltzmann distribution:

$$c_{mi,k}^{i} = c_{mA,k} \exp\left(-z^{i} \Delta \varphi_{D,k}\right)$$
(9)

where z^i is the valence of ion i. In the subcell k of the electrode, the volumetric charge density in the micropores, $\sigma_{mi,k}$, (mol mL⁻¹) rises as a result of the concentration difference between counter-ions and co-ions:

$$\sigma_{mi,k} = \sum_{i=1}^{n} z^i c^i_{mi,k} \tag{10}$$

For simplicity, in this study, we only consider a single solute of 1:1 electrolyte (e.g., NaCl), in which case eq. (10) becomes

$$\sigma_{mi,k} = -2c_{mA,k}\sinh(\Delta\varphi_{D,k}) \tag{11}$$

At the same time, $\sigma_{mi,k}$ is also related to the dimensionless Stern layer potential difference $(\Delta \varphi_{St,k})$ and the volumetric Stern layer capacitance in the micropore $(C_{St-vol,k}$, unit: F mL⁻¹):

$$\sigma_{mi,k}F = -C_{St-\nu ol,k}\Delta\varphi_{St,k}V_T \tag{12}$$

where V_T is the thermal voltage that converts the dimensionless voltage to the unit of volt (25.6 mV at 298 K). It has been shown that the volumetric Stern layer capacitance increases with charge density due to electrostatic compression(Bazant et al., 2005; Grahame, 1947; Biesheuvel and van der Wal, 2010). This relationship be can approximated using the following empirical expression:

$$C_{St-vol,k} = C_{St-vol,0} + \alpha \sigma_{mi,k}^2 \tag{13}$$

where α is an empirical coefficient (F mL⁻¹ mol²) and $C_{St-vol,0}$ is the volumetric Stern layer capacitance when the micropore charge density is zero.

2.4. Electrode channel modelling

The flow electrode consists of AC particles, CB particles and the electrolyte. Compared with film electrodes, the flow electrode has a

much smaller volume fraction of micropores and thus a much smaller microporosity, due to the low weight-to-volume fraction of AC particles. In addition, as opposed to a film electrode, the electrical conductivity of the flow electrode channel results from the conductivity of both AC particles and the electrolyte with the contribution of the electrolyte dependent on the electrolyte salinity. We propose an empirical expression to estimate the overall conductivity of the flow electrode in a subcell with this expression accounting for the conductivity of pure AC, ρ_{AC} , and the mass fraction of carbon, wt (dimensionless). The overall conductivity (ρ_{elec} , unit: S cm⁻¹) of the electrode channel is expressed as:

$$\rho_{elec} = \lambda_{s} c_{mA} (1 - wt) + \rho_{AC} wt^{\gamma}$$
(14)

where λ_s is the molar conductivity (S cm² mol⁻¹) of the solution and γ is an empirical coefficient that is independent of operating conditions. Because the flowrate of the flow electrode slurry is large in this study, we ignore the influence of the slurry flowrate in the present model. With lower slurry flowrates, however, less frequent collisions between AC particles may also lead to lower overall conductivity.

Combining the potential drop across the Stern layer and the Donnan potential, we can rewrite the overall potential drop in the electrode channel as follows:

$$V_{elec,k} = 2V_T \left(\Delta \varphi_{D,k} + \Delta \varphi_{St,k} \right) + 2I_k L_{elec} / \rho_{elec,k}$$
 (15)

The total voltage across the unit cell is the summation of all the voltage drops. Assuming the cell is symmetric, the total voltage can be represented as:

$$V_{total,k} = 2V_T \left(\Delta \varphi_{hf-sp,k} + \Delta \varphi_{\frac{m}{sp},k} + \Delta \varphi_{m,k} - \Delta \varphi_{\frac{m}{e},k} \right) + 2V_{elec,k} + I_k \cdot ESR$$
(16)

where ESR is the specific equivalent series resistance (Ω cm²) including the resistances that occur in between the current collector and the flow electrode and that in the electrical circuit. Note that in simulating the FCDI process under steady state, the cell voltage in every unit cell is the same and equal to the overall cell voltage. However, the current density varies with unit cell, of which the mean is the overall current density.

For each subcell k of the flow electrode channel, $c_{mA,k}$ and $c_{mi,k}$ are related to the ion flux $J_{ions,k}$ by the following equation (similar to eq. (1)):

$$\frac{\partial}{\partial t} \left(2p_{mA} c_{mA,k} + p_{mi} c_{mi,k} \right) = \frac{J_{ions,k}}{L_{elec}} + \frac{2p_{mA} \left(c_{mA,k} - c_{mA,k-1} \right) + p_{mi} \left(c_{mi,k} - c_{mi,k-1} \right)}{\tau_{elec}/N}$$
(17)

where τ_{elec} is the total hydraulic resistance time (HRT, unit: s) of carbon slurry in the electrode channel, which is divided by N to give the HRT in each subcell. The system of differential and algebraic equations in the model were solved numerically with MATLAB®.

3. Experimental methods

3.1. Experimental setup

The FCDI module used in this study has been described previously(He et al., 2018a). Briefly, the module consists of two

electrode-channels separated from the central spacer channel by an AEM and a CEM (AEM-Type II/CEM-Type II, FUJIFILM Europe), respectively. The dry AC powder in the flow electrode is made from 90 wt % Darco AC and 10 wt% Norit AC, both are purchased from Sigma Aldrich. The details of the AC properties are summarized in Table S2. During the operation, the positively and negatively charged electrode slurries exiting the FCDI module are mixed in a stirred tank where oppositely charged AC particles contact each other to become neutral, and the ions adsorbed inside the FCDI module are released. The electrode slurries are pumped through the serpentine channels carved in an acrylic plate. The channels have a dimension of 2 (D) \times 2 (W) mm \times 570 (L) mm. The effective contact area between the serpentine channels and the IEM is 11.9 cm² while the contact area between the current collector and the IEM is equal to 22.0 cm². The details of the FCDI cell are shown in Supplementary Information (Fig. S2&3). The feedwater is pumped through the spacer-channel for ion removal with the effluent salinity measured continuously using an inline conductivity meter.

3.2. Experimental conditions

The flow electrode was prepared by mixing Milli-Q water (18.2 M Ω cm) with different weight percentages of AC powder (2, 5 and 10 wt %). The flow electrode was charged by a DC power supply with different current densities (8.4, 16.8, 25.2 and 33.6 A m $^{-2}$). The influence of HRT (0.47, 0.69, 0.91 and 1.40 min) on the FCDI performance was investigated by changing the flowrate of feed water running through the spacer channel.

3.3. Performance evaluation

The cell voltage, current and conductivity were recorded using corresponding probes (Vernier Software & Technology, Beaverton, OR, USA) connected to a SensorDAQ. The specific energy consumption, SEC, can be defined as the energy consumped per unit volume of the product water (i.e., SEC_w):

$$SEC_{w} = A \frac{IV}{O}$$
 (18)

or per amount of salt removed (i.e., SEC_i):

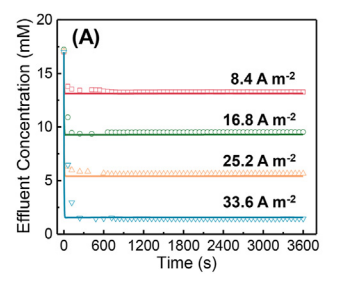
$$SEC_i = A \frac{IV}{Q(c_0 - c_D)} \tag{19}$$

where V is the cell voltage, I is the current density, A is the effective area, Q is the feed flowrate in the spacer-channel and c_0 and c_D are the concentrations of the feed (i.e., the influent) and deionized water (i.e., the effluent) stream, respectively.

Because electro-sorption and electrodialysis both occur in an FCDI process, the quantification of desalination rate is based on average salt removal rate (ASRR) instead of the average salt adsorption rate (ASAR) as used in a CDI system based on film electrodes(Nativ et al., 2017; Ma et al., 2018). The definition of ASRR is the amount of salt removed per area of IEM in a unit time:

$$ASRR = \frac{Q(c_0 - c_D)}{A} \tag{20}$$

SEC and ASRR values for both experimental data and simulation results were obtained using eqs (18)–(20) with comparison of these values used to evaluate the FCDI performance over a range of experimental conditions.



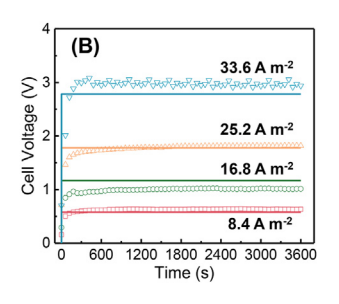


Fig. 2. Experimental results and model validation for **(A)** effluent concentration, and **(B)** cell voltage for continuous FCDI operations over 1 h. The open symbols in (A) represent concentrations converted from a pre-calibrated in-line conductivity meter. The open symbols in (B) represent the real-time cell voltages. The solid lines in both panels are results simulated with the EFE-FCDI model. This set of experiments was obtained with a FCDI containing 5% (wt/v) of AC and a spacer channel HRT of 0.69 min.

4. Results and discussion

4.1. Experimental results and model validation

A series of FCDI experiments with various operational conditions were conducted to validate the proposed model by fitting the data for effluent concentration and cell voltage/current as a function of time. A value of N = 8 is used in this study with a larger number of subcells found to provide little improvement in model fit to the experimental data. The only fitting parameters used were the coefficient γ in eq. (14) and the specific equivalent series resistance R_{esr} in eq. (16), which were adjusted to obtain a good fit of the experimentally measured effluent concentration and average current density. The values of the AC properties, such as $C_{St-vol,0}$ and α in eq. (13), are reported in the literature(Wang and Lin, 2018b; Qu et al., 2018; Dykstra et al., 2016; Zhang et al., 2015). We note that γ and ESR are the only two properties of the FCDI system and these parameters do not depend on operating conditions. Therefore, the same γ and ESR apply to all scenarios with different operating conditions presented in this study. Consequently, the FCDI model that is developed here with the fitted γ and ESR can be used for predicting performance at different operating conditions.

Experimentally, the effect of changes in three operating parameters including current density, hydraulic residence time (HRT) and carbon content were examined. In total, four values of current density, four values of spacer channel HRT and three values of carbon loading were studied. The effluent concentrations and cell voltages at various current densities are presented in Fig. 2. Although SCC FCDI is usually considered a steady-state process, the start-up of an FCDI system is still dynamic. The presence of the IEMs, however, enables an FCDI system to reach a steady-state effluent concentration in a relatively short time with the effluent concentration similar to that achieved in membrane CDI (MCDI).

Increasing the current density for the same HRT results in a decrease in the effluent concentration (Fig. 2A). At relatively high current density (33.6 A m⁻²), salt rejection as high as 92% was achieved. During the start-up stage, the cell voltage rose sharply to a stable level. Unlike the case of film-electrode CDI in which cell voltage continuously rises over time when the cell is charged at constant current, the cell voltage in SCC FCDI remains stable (Fig. 2B) because the exhausted AC particles continue to be regenerated outside the FCDI cell. Overall, the results from the EFE-FCDI model are in excellent agreement with the experimental data (of the steady-state effluent concentrations) with this agreement demonstrating the capability of the EFE-FCDI model in predicting the performance of FCDI over a range of operating conditions. Additional fittings of experimental data with the EDF-

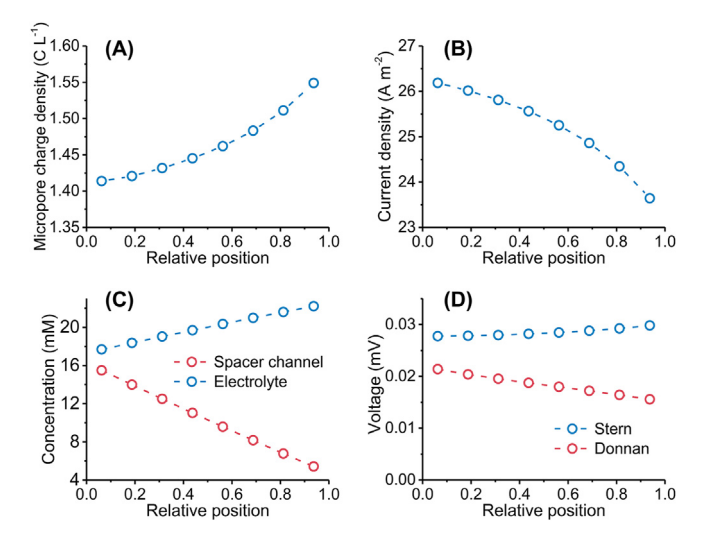


Fig. 3. Spatial variation of important properties in an FCDI cell obtained from simulation with an overall charging current density of 25.2 A m⁻² (the corresponding overall voltage is 1.78 V). The spatially-variant properties presented here include **(A)** micropore charge density, **(B)** local current density, **(C)** local salt concentrations in the spacer channel (red) and flow electrode channel (blue, excluding micropores), and **(D)** local Stern and Donnan potential drops. In this simulation, the AC loading is 5% (w/v) and the HRT of the spacer stream is 0.69 min. The x-axis represents the relative position along the flow direction of the feed water and flow electrode streams. (For interpretation of the references to colour in this figure legend, the reader is referred to the Web version of this article.)

FCDI model are provided in the Supporting Information (Fig. S1).

CDI processes based on film electrodes are dynamic, i.e., there are always certain key system parameters that vary temporally. For example, when charging a CDI process at constant voltage (CV), the current density and effluent salinity both change over time due to the temporal variation in the driving force for ion transport. Alternatively, when charging a CDI process at constant current (CC), the cell voltage has to rise over time to offset the build-up of Stern and Donnan potentials in the EDL, so that a constant driving force for ion transport can be maintained. In contrast, there is no temporal variation of parameters in a FCDI process except for the short start-up stage, even though the same build-up of Stern and Donnan potentials in the EDL of the AC still occur as AC particles flow along the electrode channel and accumulate additional ions in their micropores. In essence, the constant movement of the electrodes converts the temporal variations of the system to spatial variations. The spatial variations of various system properties are illustrated in Fig. 3. These properties include the volumetric micropore charge density, σ_{mi} (Fig. 3A), the current density (Fig. 3B), the salt concentration in the spacer channel and the solution phase of the flow electrode channel (Fig. 3C) and the Stern and Donnan potentials (Fig. 3D).

CDI systems with film electrodes are typically charged using CC or CV mode. The reason for specifying what should be constant is precisely because not all properties can remain temporally constant. Specifically, as charging proceeds, the current diminishes in CV mode while the cell voltage rises in CC mode. For FCDI with a single pair of current collectors, however, everything is temporally constant, and there is only one cell voltage for the FCDI system as a whole. On the other hand, the current density varies spatially along the water flow direction as the water is desalinated (Fig. 3B). Therefore, referring to an FCDI operation as CC or CV is not meaningful as FCDI always possesses both characteristics. However, if we follow a thin slab of AC slurry in the flow electrode channel, that flowing portion of the electrode has the characteristic of CV charging, as the corresponding current density decreases over time

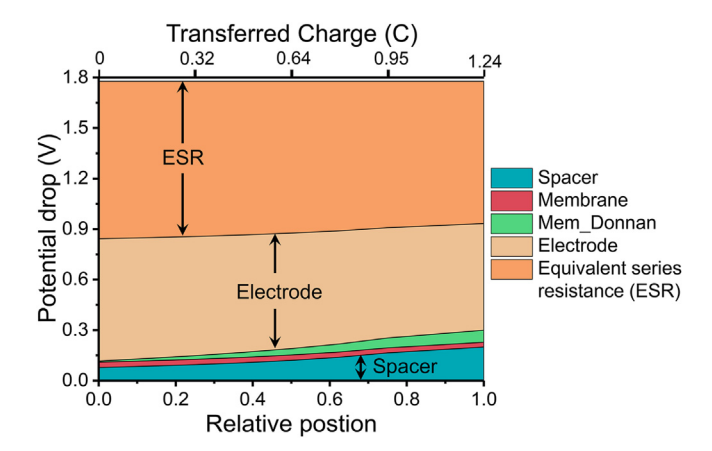


Fig. 4. Spatial distribution of contributions to potential drop in an FCDI module determined using the EFE-FCDI model. In this simulation, the feed salinity is reduced from 17 mM to 5.4 mM with a spacer-channel HRT of 0.69 min. The cell voltage is 1.78 V and the overall current density is 25.2 A cm⁻². The overall cell voltage is divided into seven components as described in the text. However, only five components are presented in this figure because the Stern potential in the micropores and the Donnan potential between the micropores and macropores are comparatively negligible (see Fig. 3D). The equivalent series resistance (ESR) is a fitting parameter that enables the modelled current density and effluent concentration to match the experimental results at different cell voltages, which are invariant with operational conditions.

(temporally) and along the electrode channel (spatially) (Fig. 3B).

To futher illustrate that an FCDI cell has both CC and CV characteristics, we simulate the distribution of potential drops in different components at different positions of the FCDI module (Fig. 4). In a typical EFE-FCDI model, these potential drops should include seven components including the Stern potential in the micropores, the Donnan potential between the micropores and macropores, the potential drop in the flow electrode chamber (electrode), the potential drop across the IEMs (membrane), the sum of the Donnan potential drops across the two interfaces of the IEMs (mem_Donnan), the potential drop across the spatial channel (spacer) and the potential drop due to the series resistance (Ma et al., 2018). However, the results from our simulation suggest that the Stern potential in the micropores and the Donnan potential between the micropores and macropores are both negligible compared to other contributions (Fig. 3D). As such, these potentials are not included in Fig. 4.

Because there can only be one potential for a current collector, the cell voltage is also spatially independent. Therefore, the sum of the all potential drops across the two current collectors is also spatially constant (1.8 V in this case). However, the individual contributions to the overall potential drop vary along the module as more charge is transferred (top axis in Fig. 4) and more salts are removed from the feed stream. Specifically, the potential drop across the IEMs and the potential drop due to series resistance both decrease as the local current density decreases along the feed stream flow. In addition, the decrease in salt concentration in the spacer channel and increase in the flow electrode channel results in changes in the electrical resistance and thus the potential drop in the respective channels (Fig. 4).

4.2. Performance evaluation of FCDI

The effects of operating conditions on the FCDI performance metrics were investigated over a wide range of operating conditions using both experimental and modeling approaches. We first investigated the impact of current density on the average salt removal rate, ASRR, and specific energy consumption, SEC. As the current density increases from 8.4 to 33.6 A cm⁻², ASRR increases

linearly from 5.0 to 20.9 mmol cm⁻² min⁻¹ (Fig. 5A). Notably, the *ASRR* of FCDI is higher than the average salt adsorption rate in most MCDI processes (usually lower than 10 mmol cm⁻² min⁻¹). Increasing current density also results in greater energy consumption. Specifically, *SEC* increases linearly from 0.06 to 0.28 J μmol⁻¹ when the current density quadrupled from 8.4 to 33.6 A cm⁻² (Fig. 5A). These results reflect the intrinsic tradeoff between desalination rate and energy efficiency as discussed in several recent papers (Wang and Lin, 2019, 2018b; Wang et al., 2019; Hawks et al., 2018b; Hemmatifar et al., 2018). We also note that results from the numerical simulation are in remarkably good agreement with the experimental results.

With a fixed current density, increasing HRT results in a reduction in effluent salinity and an increase in salt rejection. However, HRT has a negligible impact on the desalination rate (Fig. 5B), which is unsurprising because ASRR is roughly proportional to current density as long as charge efficiency remains similar. In comparison, the energy consumption is slightly more sensitive to HRT, with SEC increasing from 0.10 to 0.16 J μmol^{-1} when HRT increases from 0.47 to 1.4 min (Fig. 5B). SEC increases mainly because a longer HRT results in greater reduction of the feed salinity and thus a lower average feed salinity which, in turn, leads to a higher average feed channel resistance and a higher overall cell resistance.

A distinct characteristic of FCDI, as opposed to conventional CDI with film electrodes, is that the carbon content of the electrode is adjustable. Increasing the AC loading from 2 to 10% results in a significant reduction in SEC from 0.35 to 0.10 I μ mol⁻¹ (Fig. 5C). This improvement in energy efficiency is attributable to the increase of overall conductivity of the flow electrode channel, as the charge transfer is enhanced as more frequent collisions between AC particles occur at higher AC loading. However, the increase of AC loading also comes with the practical disadvantage that circulating the AC slurry in the electrode channel becomes more challenging (i.e., larger pressure drop and more prone to clogging) as the viscosity increases with AC loading. While this practical challenge is not specifically investigated in the current study, the caveats of increasing the carbon content of the flow electrode should not be overlooked in practical system design. On the other hand, increasing the carbon content does not affect the ASRR if the current density is maintained the same. From all three series of experiments, it is clear that while SEC may depend on operational and system parameters in different ways, the desalination rate is only a function of current density.

4.3. Performance tradeoff in FCDI

Recent studies have identified the importance of quantifying the intrinsic tradeoff between energy efficiency and desalination rate for desalination systems (Wang and Lin, 2018b; Hawks et al., 2018b; Liu and Smith, 2018; Lin and Elimelech, 2017). Specifically, the performance tradeoff curve, in this case relating the SEC and ASRR, can serve as a useful tool for systematic comparison between operations and for technoeconomic analysis of FCDI. Here, we construct the performance tradeoff curves using the experimentally validated EFE-FCDI model to elucidate the impacts of operating conditions on the overall system performance. The performance tradeoff curves were simulated by simultaneously varying the applied voltage and the flowrate of the feed stream so that an identical effluent concentration is achieved for every point in a performance tradeoff curve (Fig. 6A). We use the experimentally validated EFE-FCDI model to simulate performance tradeoff curves for FCDI systems with different carbon contents in the flow electrode (Fig. 6B), feed concentrations (Fig. 6C and E) and diluted effluent concentrations (Fig. 6D and F). The FCDI performance is

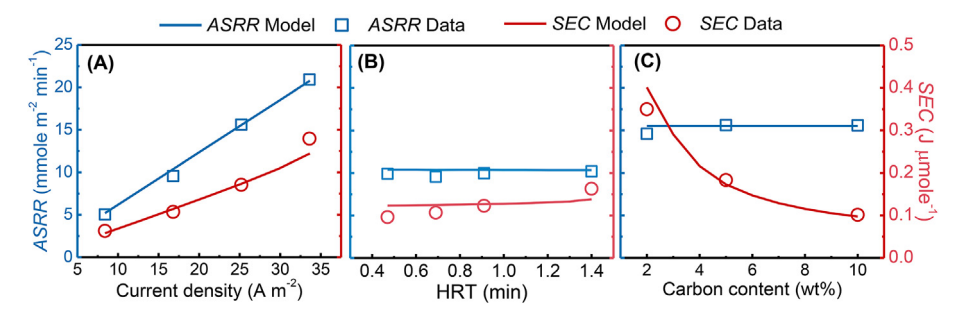


Fig. 5. Experimental and modelling results of FCDI performance for different operating conditions. The influence of current density (A) was examined when the HRT was set at 0.69 min and the carbon content was 5 wt%. When studying the effects of HRT (B), a current density of 16.8 A m⁻² was applied to an FCDI cell with carbon content of 5 wt%. Three levels of carbon loading were investigated (C) using a cell voltage of 1.78 V, consequential current density of 25.2 A m⁻² and HRT of the spacer stream of 0.69 min.

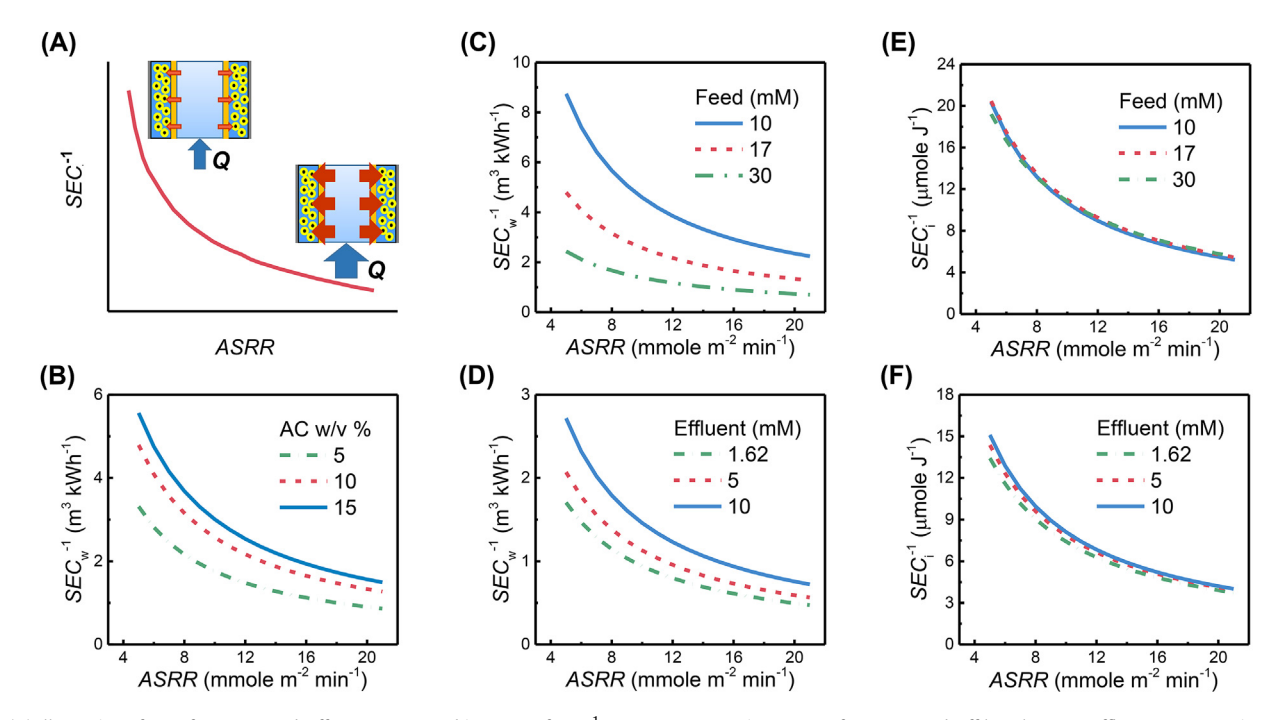


Fig. 6. (A) Illustration of a performance tradeoff curve expressed in terms of SEC_w^{-1} vs. ASRR. Every point on a performance tradeoff has the same effluent concentration, which is achieved by simultaneous adjustment of both feed stream flowrate and cell voltage (which affects current). (B) Simulated performance tradeoff curves for FCDI with carbon loading in the flow electrode channel. Here, the influent and effluent concentrations are 17 mM and 1.62 mM, respectively. (C) Simulated performance tradeoff curves for FCDI with different feed concentrations. Here, the effluent concentration is 1.62 mM and the carbon content is 10%. (D) simulated performance tradeoff curves for FCDI with different diluted effluent concentrations. Here, the influent concentration is 30 mM and the carbon content is 5%. (E) and (F) are the same as (C) and (D), respectively, except that the energy efficiency is expressed in terms of SEC_1^{-1} where SEC_1^{-1} where SEC_1^{-1} where SEC_1^{-1} where SEC_1^{-1} where SEC_1^{-1} where SEC_1^{-1} is the energy consumed to remove an ion. The results presented in this figure are simulated using the EFE-FCDI model and have not been validated using experiments performed in these specific conditions.

quantified by performance tradeoff curves that relate the inverse of $SEC_{\rm w}$ (or $SEC_{\rm i}$) and ASRR which quantify the kinetic and energetic efficiencies, respectively. As a rule-of-thumb, a performance tradeoff curve that is in the upper-right position of a $SEC_{\rm w}^{-1}$ (or $SEC_{\rm i}^{-1}$) vs. ASRR plot is preferred.

In general, increasing the carbon content leads to kinetically and energetically more favorable FCDI operation (Fig. 6B), mainly due to increased electrical conductivity. The positive impact of increasing the carbon content is particularly salient when the carbon conent is low. For instance, increasing the carbon content from 5 to 10% dramatically enhances $SEC_{\rm w}^{-1}$. However, further increasing the carbon content from 10 to 15%, by the same increment of 5%, has a considerably smaller effect in further enhancing the energetic and kinetic efficiencies. The dwindling impact of increasing carbon content when the carbon content is releatively high can be explained by the inverse relationship between electrical resistance and electrical conductivity; i.e., increasing the electrical

conductivity has a much stronger effect in reducing the electrical resistance when the electrical conductivity is low compared to the effect when it is high. A flow electrode with high carbon content becomes more viscous and prone to clogging, which increases the pumping energy for circulation (not considered in this analysis) and renders practical FCDI operation considerably more challenging. Considering the significant detrimental impacts on operation and diminishing return on reducing flow channel resistance of increasing carbon content, the carbon content in the flow electrode should be limited to a certain level.

Increasing the feed concentration (Fig. 6C) or reducing the effluent concentration (Fig. 6D) leads to "less favorable" performance as indicated by up-right shift of the performance tradeoff curves " $SEC_{\rm w}^{-1}$ vs. ASRR". However, this is unsurprising because in either case more salts are removed from the feed water which should supposedly result in high energy consumption per volume of the treated water. When we normalize the energy by the amount

of salt removed, instead of the volume of water treated, the new performance tradeoff curves " SEC_1^{-1} vs. ASRR" suggest that changing either the feed or the effluent concentration has minmal impact on the system performance (Fig. 6E and F). In theory, a feed stream with a lower salinity has a higher electrical resistance, which consequently results in compromised performance. This effect is more salient with reduced effluent concentration than with reduced feed concentration, because resistance is roughly inversely proportional to salinity and the impact of salinity is thus stronger in the low salinity range. Indeed, compared to a nearly unobservable impact of feed concentration on performance (Fig. 6E), the impact of effluent concentration is more obvious (Fig. 6F). However, neither impact is significant because the spacer channel resistance only has a small contribution to the overall resistance according to the breakdown shown in Fig. 4.

5. Conclusions and implications

While the microscopic behavior of the flow electrodes in FCDI is very complex and requires multi-phase hydrodynamic modeling for full elucidation, we have demonstrated in this work that the system level behavior of FCDI can be satisfactorily described using an equivalent film electrode (EFE) model where the flow electrode is simply treated as a moving film electrode. Not only does the EFE model yield a very good description of the experimental data, it can also be employed for performance prediction because the model does not have any operation-specific fitting parameters. As such, the EFE-FCDI model can be employed for designing and optimizing FCDI systems. It can also be used for theoretical investigation to enhance our fundamental understanding of FCDI because it enables the analysis of the spatial distribution of the important properties in the FCDI cell and the breakdown of energy loss in different parts of the system. Our analysis based on performance tradeoff curves simulated using the EFE-FCDI model suggests that AC content in the flow electrode channel has the largest impact on system performance evaluated based on energy consumption per ion removed, whereas both the feed salinity and the target effluent salinity have negligible impact.

Declaration of competing interest

The authors declare that they have no known competing financial interests or personal relationships that could have appeared to influence the work reported in this paper.

Acknowledgement

L.W. and S.L. acknowledge the support by the Natural Science Foundation via research grant 1739884. C.Z. and T.D.W. acknowledge the funding support from the Australian Research Council and Beijing Origin Water through ARC Linkage Grant LP170101180. Support for C.Z. through UNSW Faculty Postdoctoral Writing Fellowship is gratefully acknowledged.

Appendix A. Supplementary data

Supplementary data to this article can be found online at https://doi.org/10.1016/j.watres.2020.115917.

References

- Bazant, M.Z., Chu, K.T., Bayly, B.J., 2005. Current-voltage relations for electrochemical thin films. SIAM J. Appl. Math. 65 (5), 1463–1484.
- Biesheuvel, P.M., Zhao, R., Porada, S., van Der Wal, A., 2011. Theory of membrane capacitive deionization including the effect of the electrode pore space. J. Colloid Interface Sci. 360 (1), 239–248.

- Biesheuvel, P.M., van der Wal, A., 2010. Membrane capacitive deionization. J. Membr. Sci. 346 (2), 256–262.
- Cho, Y., Yoo, C.-Y., Lee, S.W., Yoon, H., Lee, K.S., Yang, S., Kim, D.K., 2019. Flow-electrode capacitive deionization with highly enhanced salt removal performance utilizing high-aspect ratio functionalized carbon nanotubes. Water Res. 151, 252–259.
- Dennison, C.R., Beidaghi, M., Hatzell, K.B., Campos, J.W., Gogotsi, Y., Kumbur, E.C., 2014. Effects of flow cell design on charge percolation and storage in the carbon slurry electrodes of electrochemical flow capacitors. J. Power Sources 247, 489–496.
- Dykstra, J.E., Zhao, R., Biesheuvel, P.M., van der Wal, A., 2016. Resistance identification and rational process design in Capacitive Deionization. Water Res. 88, 358–370.
- Farmer, J.C., Fix, D.V., Mack, G.V., Pekala, R.W., Poco, J.F., 1996. Capacitive deionization of NaCl and NaNO3 solutions with carbon aerogel electrodes. J. Electrochem. Soc. 143 (1), 159–169.
- Gendel, Y., Rommerskirchen, A.K.E., David, O., Wessling, M., 2014. Batch mode and continuous desalination of water using flowing carbon deionization (FCDI) technology. Electrochem. Commun. 46, 152–156.
- Grahame, D.C., 1947. The electrical double layer and the theory of electrocapillarity. Chem. Rev. 41 (3), 441–501.
- Hatzell, K.B., Boota, M., Gogotsi, Y., 2015. Materials for suspension (semi-solid) electrodes for energy and water technologies. Chem. Soc. Rev. 44 (23), 8664–8687
- Hawks, S.A., Knipe, J.M., Campbell, P.G., Loeb, C.K., Hubert, M.A., Santiago, J.G., Stadermann, M., 2018a. Quantifying the flow efficiency in constant-current capacitive deionization. Water Res. 129, 327–336.
- Hawks, S.A., Ramachandran, A., Porada, S., Campbell, P.G., Suss, M.E., Biesheuvel, P.M., Santiago, J.G., Stadermann, M., 2018b. Performance Metrics for the Objective Assessment of Capacitive Deionization Systems. Water Research.
- He, C., Ma, J., Zhang, C., Song, J., Waite, T.D., 2018a. Short-circuited closed-cycle operation of flow-electrode CDI for brackish water softening. Environ. Sci. Technol. 52 (16), 9350–9360.
- He, F., Biesheuvel, P.M., Bazant, M.Z., Hatton, T.A., 2018b. Theory of water treatment by capacitive deionization with redox active porous electrodes. Water Res. 132, 282–291.
- Hemmatifar, A., Stadermann, M., Santiago, J.G., 2015. Two-dimensional porous electrode model for capacitive deionization. J. Phys. Chem. C 119 (44), 24681–24694.
- Hemmatifar, A., Ramachandran, A., Liu, K., Oyarzun, D.I., Bazant, M.Z., Santiago, J.G., 2018. Thermodynamics of Ion Separation by Electrosorption. Environmental Science & Technology.
- Jeon, S.I., Park, H.R., Yeo, J.G., Yang, S., Cho, C.H., Han, M.H., Kim, D.K., 2013. Desalination via a new membrane capacitive deionization process utilizing flow-electrodes. Energy Environ. Sci. 6 (5), 1471–1475.
- Jeon, S.I., Yeo, J.G., Yang, S., Choi, J., Kim, D.K., 2014. Ion storage and energy recovery of a flow-electrode capacitive deionization process. J. Mater. Chem. 2 (18), 6378–6383.
- Ji, F., Wang, L., Yang, J.S., Wu, X., Li, M.Q., Jiang, S.L., Lin, S.H., Chen, Z., 2019. Highly compact, free- standing porous electrodes from polymer- derived nanoporous carbons for efficient electrochemical capacitive deionization. J. Mater. Chem. 7 (4), 1768–1778.
- Karzar-Jeddi, M., Luo, H.X., Cummings, P.T., Hatzell, K.B., 2019. Computational modeling of particle hydrodynamics and charging process for the flowable electrodes of carbon slurry. J. Electrochem. Soc. 166 (12), A2643—A2653.
- Liang, P., Sun, X.L., Bian, Y.H., Zhang, H.L., Yang, X.F., Jiang, Y., Liu, P.P., Huang, X., 2017. Optimized desalination performance of high voltage flow-electrode capacitive deionization by adding carbon black in flow-electrode. Desalination 420, 63–69.
- Lin, S.H., Elimelech, M., 2017. Kinetics and energetics trade-off in reverse osmosis desalination with different configurations. Desalination 401, 42–52.
- Liu, S.Z., Smith, K.C., 2018. Quantifying the trade-offs between energy consumption and salt removal rate in membrane-free cation intercalation desalination. Electrochim. Acta 271, 652–665.
- Luo, K., Niu, Q., Zhu, Y., Song, B., Zeng, G., Tang, W., Ye, S., Zhang, J., Duan, M., Xing, W., 2020. Desalination behavior and performance of flow-electrode capacitive deionization under various operational modes. Chem. Eng. J. 124051.
- Ma, J.X., He, C., He, D., Zhang, C.Y., Waite, T.D., 2018. Analysis of capacitive and electrodialytic contributions to water desalination by flow-electrode CDI. Water Res. 144, 296–303.
- Ma, J., Zhang, C., Yang, F., Zhang, X., Suss, M., Huang, X., Liang, P., 2019. Carbon black flow-electrode enhanced electrochemical desalination using single cycle operation. Environ. Sci. Technol.
- Moreno, D., Hatzell, M.C., 2018. Influence of feed-electrode concentration differences in flow-electrode systems for capacitive deionization. Ind. Eng. Chem. Res. 57 (26), 8802–8809.
- Nativ, P., Badash, Y., Gendel, Y., 2017. New insights into the mechanism of flowelectrode capacitive deionization. Electrochem. Commun. 76, 24–28.
- Porada, S., Zhao, R., van der Wal, A., Presser, V., Biesheuvel, P.M., 2013a. Review on the science and technology of water desalination by capacitive deionization. Prog. Mater. Sci. 58 (8), 1388–1442.
- Porada, S., Borchardt, L., Oschatz, M., Bryjak, M., Atchison, J.S., Keesman, K.J., Kaskel, S., Biesheuvel, P.M., Presser, V., 2013b. Direct prediction of the desalination performance of porous carbon electrodes for capacitive deionization. Energy Environ. Sci. 6 (12), 3700–3712.

- Porada, S., Weingarth, D., Hamelers, H.V.M., Bryjak, M., Presser, V., Biesheuvel, P.M., 2014. Carbon flow electrodes for continuous operation of capacitive deionization and capacitive mixing energy generation. J. Mater. Chem. 2 (24), 9313–9321.
- Qin, M., Deshmukh, A., Epsztein, R., Patel, S.K., Owoseni, O.M., Walker, W.S., Elimelech, M., 2019. Comparison of energy consumption in desalination by capacitive deionization and reverse osmosis. Desalination 455, 100–114.
- Qu, Y.T., Campbell, P.G., Hemmatifar, A., Knipe, J.M., Loeb, C.K., Reidy, J.J., Hubert, M.A., Stadermann, M., Santiago, J.G., 2018. Charging and transport dynamics of a flow-through electrode capacitive deionization system. J. Phys. Chem. B 122 (1), 240–249.
- Rommerskirchen, A., Linnartz, C.J., Muller, D., Willenberg, L.K., Wessling, M., 2018a. Energy recovery and process design in continuous flow electrode capacitive deionization processes. ACS Sustain. Chem. Eng. 6 (10), 13007–13015.
- Rommerskirchen, A., Gendel, Y., Wessling, M., 2015. Single module flow-electrode capacitive deionization for continuous water desalination. Electrochem. Commun. 60, 34–37.
- Rommerskirchen, A., Ohs, B., Hepp, K.A., Femmer, R., Wessling, M., 2018b. Modeling continuous flow-electrode capacitive deionization processes with ion-exchange membranes. J. Membr. Sci. 546, 188–196.
- Suss, M.E., Porada, S., Sun, X., Biesheuvel, P.M., Yoon, J., Presser, V., 2015. Water desalination via capacitive deionization: what is it and what can we expect from it? Energy Environ. Sci. 8 (8), 2296–2319.
- Suss, M.E., Baumann, T.F., Bourcier, W.L., Spadaccini, C.M., Rose, K.A., Santiago, J.G., Stadermann, M., 2012. Capacitive desalination with flow-through electrodes. Energy Environ. Sci. 5 (11), 9511–9519.
- Suss, M.E., Biesheuvel, P.M., Baumann, T.F., Stadermann, M., Santiago, J.G., 2014. In situ spatially and temporally resolved measurements of salt concentration between charging porous electrodes for desalination by capacitive deionization. Environ. Sci. Technol. 48 (3), 2008–2015.
- Tang, W., Liang, J., He, D., Gong, J., Tang, L., Liu, Z., Wang, D., Zeng, G., 2019b. Various cell architectures of capacitive deionization: recent advances and future trends. Water Res. 150, 225–251.
- Tang, W., Wang, X., Zeng, G., Liang, J., Li, X., Xing, W., He, D., Tang, L., Liu, Z., 2019a. Electro-assisted adsorption of Zn(II) on activated carbon cloth in batch-flow mode: experimental and theoretical investigations. Environ. Sci. Technol. 53 (5), 2670.

- Wang, Li, Liang, Yuanzhe, Zhang, Li, 2020. Enhancing Performance of Capacitive Deionization with Polyelectrolyte-Infiltrated Electrodes: Theory and Experimental Validation. Environ. Sci. Technol. 54 (9), 5874–5883. https://doi.org/ 10.1021/acs.est.9b07692.
- Wang, L., Lin, S.H., 2018a. Membrane capacitive deionization with constant current vs constant voltage charging: which is better? Environ. Sci. Technol. 52 (7), 4051–4060.
- Wang, L., Lin, S.H., 2018b. Intrinsic tradeoff between kinetic and energetic effi-
- Wang, L., Lin, S.H., 2019. Theoretical framework for designing a desalination plant based on membrane capacitive deionization. Water Res. 158, 359–369.
- Wang, L., Biesheuvel, P.M., Lin, S., 2017. Reversible thermodynamic cycle analysis for capacitive deionization with modified donnan model. J. Colloid Interface Sci.
- Wang, L., Dykstra, J.E., Lin, S.H., 2019. Energy efficiency of capacitive deionization. Environ. Sci. Technol. 53 (7), 3366–3378.
- Yang, S., Choi, J., Yeo, J.G., Jeon, S.I., Park, H.R., Kim, D.K., 2016. Flow-electrode capacitive deionization using an aqueous electrolyte with a high salt concentration. Environ. Sci. Technol. 50 (11), 5892–5899.
- Yang, S., Kim, H., Jeon, S.I., Choi, J., Yeo, J.G., Park, H.R., Jin, J., Kim, D.K., 2017. Analysis of the desalting performance of flow-electrode capacitive deionization under short-circuited closed cycle operation. Desalination 424, 110–121.
- Zhang, C.Y., Ma, J.X., Song, J.K., He, C., Waite, T.D., 2018. Continuous ammonia recovery from wastewaters using an integrated capacitive flow electrode membrane stripping system. Environ. Sci. Technol. 52 (24), 14275–14285.
- Zhang, C.Y., Ma, J.X., Waite, T.D., 2019. Ammonia-rich solution production from wastewaters using chemical-free flow-electrode capacitive deionization. ACS Sustain. Chem. Eng. 7 (7), 6480–6485.
- Zhang, J., Tang, L., Tang, W., Zhong, Y., Luo, K., Duan, M., Xing, W., Liang, J., 2020. Removal and recovery of phosphorus from low-strength wastewaters by flow-electrode capacitive deionization. Separ. Purif. Technol. 237, 116322.
- Zhang, W.L., Lin, H.B., Lu, H.Y., Liu, D.C., Yin, J., Lin, Z.Q., 2015. On the electrochemical origin of the enhanced charge acceptance of the lead-carbon electrode. J. Mater. Chem. 3 (8), 4399–4404.
- Zhao, R., Biesheuvel, P.M., van der Wal, A., 2012. Energy consumption and constant current operation in membrane capacitive deionization. Energy Environ. Sci. 5 (11), 9520–9527.